Quantitative Description of Metal Center Organization and Interactions in Single-Atom Catalysts

Kevin Rossi, Andrea Ruiz-Ferrando, Dario Faust Akl, Victor Gimenez Abalos, Javier Heras-Domingo, Romain Graux, Xiao Hai, Jiong Lu, Dario Garcia-Gasulla, Nuria López*, Javier Pérez-Ramírez*, Sharon Mitchell*

K. Rossi, D. Faust Akl, J. Pérez-Ramírez, S. Mitchell

Institute for Chemical and Bioengineering, Department of Chemistry and Applied Biosciences, ETH Zurich, Vladimir-Prelog-Weg 1, 8093 Zurich, Switzerland

E-mail: jpr@chem.ethz.ch, msharon@chem.ethz.ch

A. Ruiz-Ferrando, J. Heras Domingo, N. López

Institute of Chemical Research of Catalonia, Avenida Països Catalans 16, 43007 Tarragona, Spain

E-mail: nlopez@iciq.es

A. Ruiz-Ferrando

Departament de Química Física i Inorgànica, Universitat Rovira i Virgili, Carrer de Marcellí Domingo 1, 43007 Tarragona, Spain

V. Gimenez, D. Garcia-Gasulla

Barcelona Supercomputing Center, Plaça d'Eusebi Güell 1-3, 08034 Barcelona, Spain

X. Hai, J. Lu

Department of Chemistry, National University of Singapore, Science Drive 3, Singapore, Singapore

J. Lu

Centre for Advanced 2D Materials and Graphene Research Centre, National University of Singapore, Science Drive 2, Singapore, Singapore

J. Lu

Institute for Functional Intelligent Materials, National University of Singapore, Science Drive 2, Singapore, Singapore

Abstract

Ultra-high-density single-atom catalysts (UHD-SACs) present unique opportunities for harnessing cooperative effects between neighboring metal centers. However, the lack of tools to establish correlations between the density, type, and arrangement of the isolated metal atoms with the support surface properties hinders efforts to engineer advanced material architectures. Here, we precisely describe the metal center organization in various mono- and multimetallic UHD-SACs based on nitrogen-doped carbon (NC) supports by coupling transmission electron microscopy with tailored machine-learning methods (released as a user-friendly web app) and density functional theory simulations. Our approach quantifies the non-negligible presence of multimers with increasing atom density, characterizes the size and shape of these low-nuclearity clusters, and identifies surface atom density criteria to ensure isolation. Further, it provides previously inaccessible experimental insights into coordination site arrangements in the NC host, uncovering a repulsive interaction that influences the disordered distribution of metal centers in UHD-SACs. This observation holds in multimetallic systems, where chemically-specific analysis quantifies the degree of intermixing. These fundamental

WILEY-VCH

insights into the materials chemistry of single-atom catalysts are crucial for designing catalytic systems with superior reactivity.

1. Introduction

Designing materials with atomically-precise architectures has become a cutting-edge research area with broad applications in electronics, energy storage, and catalysis.[1-2] Single-atom catalysts (SACs) exemplify this approach, aiming to maximize active metal atom accessibility by minimizing metal ensemble sizes. This control offers numerous advantages, from unlocking novel functionality to enhancing resource utilization. SACs have demonstrated exceptional efficiency and unique reactivity patterns in specific applications compared to catalytic materials containing supported nanoparticles.[3-8]

In recent years, the design of SACs has evolved from merely stabilizing isolated metal atoms to engineering precise metal environments. This shift encompasses tailoring interactions with supports, controlling the type and degree of ligation of metal centers, and manipulating their spatial organization.[1-9] Different metal center arrangements exist, from distant and isolated to proximal and interacting, with distinct potential influences and participations in catalytic cycles (**Figure 1a**). Inadequate synthesis conditions may also result in the coexistence of clusters such as dimers and other multimeric species in SACs. Interest is growing in structures integrating closely positioned metal centers, as seen in dual-atom catalysts,[10,11] which can exhibit distinct catalytic behaviors and cooperative effects (Figure S1, Supporting Information).[10-21] Achieving control over metal center proximity in SACs requires advanced synthesis methods that yield high surface coverages, such as those found in ultra-high-density SACs (UHD-SACs).[12] Factors such as the number, type, and arrangement of metal anchoring sites in the support, the adsorption properties of the metal centers, and the synthesis conditions can all influence metal center organization (Figure 1b).[12-15,22-24]

Characterizing metal center organization in SACs heavily relies on advanced microscopy techniques like aberration-corrected scanning transmission electron microscopy (AC-STEM). However, current approaches primarily focus on visually comparing metal centers dispersion, with limited attempts to

extract additional quantitative information, for example, on metal atom surface density and proximity. Moreover, the statistical robustness of the observations derived has been hampered by the limited sampling, related to the small field of view of AC-STEM images (typically below 100 nm^2) and the time-consuming nature of manual atom detection, with typical analyses considering 1-2 images per specimen. Furthermore, atom detections have traditionally relied on the manual inspection of images by domain-experts, which are prone to biases due to differences in visual perception, particularly concerning the contrast between the single atoms and the support material. This limitation is exacerbated when analyzing multimetallic systems, where classifying distinct atoms based on their relative contrast becomes
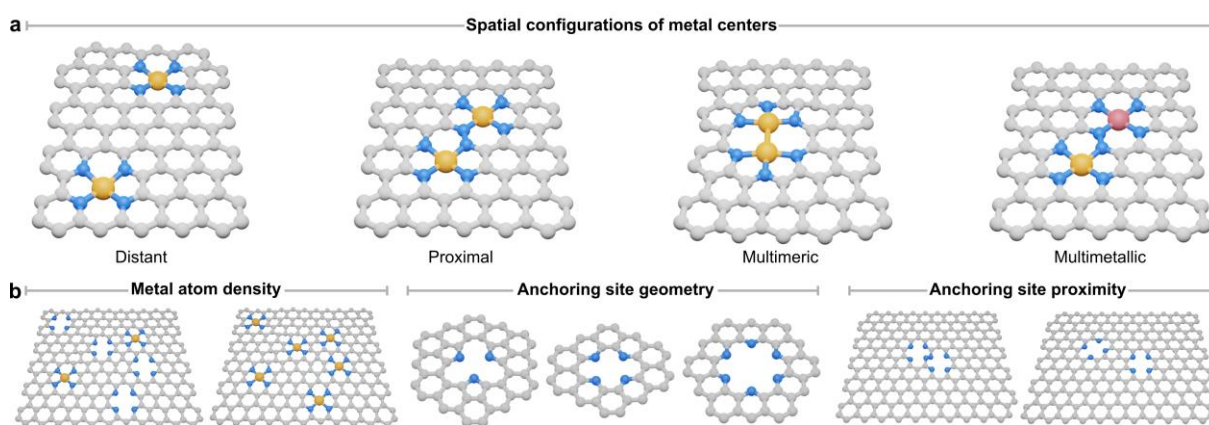

Figure 1. a, The spatial arrangement of metal centers in SACs spans a variety of geometries. In distant configurations, metal centers are well-isolated and, in principle, non-interacting. In proximal configurations, multiple metal centers are located within short distances (a few atoms separation), but do not form metal-metal bonds, and are thus still classified as single atoms. The organizational complexity increases in SACs containing multiple metal types. **b**, Various structural features of SACs can impact the arrangement of metal centers, including the proximity and geometry of anchoring sites, preferential adsorption of metal centers in specific host coordination motifs, and the surface density of deposited metal atoms. Control and optimization of these properties could enable superior catalytic properties in SACs.

WILEY-VCH

challenging. The absence of standardized approaches and potential arbitrariness in detection decisions further hinder informative analysis.

In this context, machine learning methods offer a solution, enabling standardized structure characterization, automated imaging conditions optimization, and unbiased model selection, across various disciplines, including materials science.[25-37] While machine learning has been applied for tasks like denoising,[33] shape classification,[34,35] segmentation,[36,37] and atom detection.[38] quantitative frameworks for interrogating metal center organization in SACs have lagged behind.

In this work, we bridge this knowledge gap by combining microscopy, unsupervised and supervised machine-learning methods, and numerical tools to quantitatively characterize metal center identity, spatial organization, and interactions in mono- and multimetallic UHD-SACs, across a range of surface atom densities. After efficient metal center detection facilitated by machine learning, we estimate the number of atoms in low-nuclearity clusters, analyze their geometry, quantify metal dispersion using pair distance statistics, and assess short- and long-range ordering, also with chemical specificity. Our analysis of these structural descriptors, establishes criteria for metal center isolation and characterizes nearest neighbor distance distributions as a function of the metal surface density. Density functional theory simulations support our findings and enable quantification of geometric and electronic structure contributions to interatomic interactions determining metal center spatial organization. To promote standardized characterization and analysis, we release a user-friendly web app for automated characterization, as well as software and simulations input/output in open-source repositories. This approach advances fundamental understanding of SAC chemistry and enhances the design of catalytic materials for targeted conversion processes, offering a basis for quantitative structure-performance relationships.

2. Results and Discussion

2.1. Single-Atom and Multimer Detection

We focus on UHD-SACs comprising metal atoms adsorbed on nitrogen-doped carbon (NC) as the most commonly used host material.[1] The use of high atom densities, with occupation of virtually all surface

5

WILEY-VCH

coordination sites, presents a realistic scenario for systems where cooperative effects may occur but presents significant challenges for establishing the degree of site isolation. We account for various degrees of atom detection complexity by considering widely studied catalytic metals (Rh, Ni, Pd, and Pt) that exhibit distinct contrasts in scanning transmission electron microscopy (STEM) imaging. To ensure a robust statistical analysis, we consider multiple images containing over 40'000 metal centers.

Reflecting common experimental practice, the operator carefully determines the conditions for capturing UHD-SAC images to maximize the visibility of individual atoms (**Figure 2a**). For instance, the imaging of Ni samples used a higher accelerating voltage (200 kV) compared to other metals (80 kV) to improve atomic contrast. Dwell time settings are varied to balance achieving sufficient contrast and minimizing potential sample degradation or shifting during image acquisition. The magnifications used for imaging, expressed as nm px^{-1}, cover a range where the atomically resolved isolated features are well visible. This non-standardized data set differs from previous atom detection efforts,[38] which precisely controlled the acquisition conditions, including scanned image dimensions and pixel size. Analysis of recent literature shows that full details of acquisition parameters are rarely reported (Table S1, Supporting Information), but the range that we study (Figure S2b) are representative of typical imaging conditions.

With the goal of rapid and standardized atom detection (Figure 2b), we develop a customized workflow that consists of both supervised and unsupervised elements (Figure S2a, Supporting
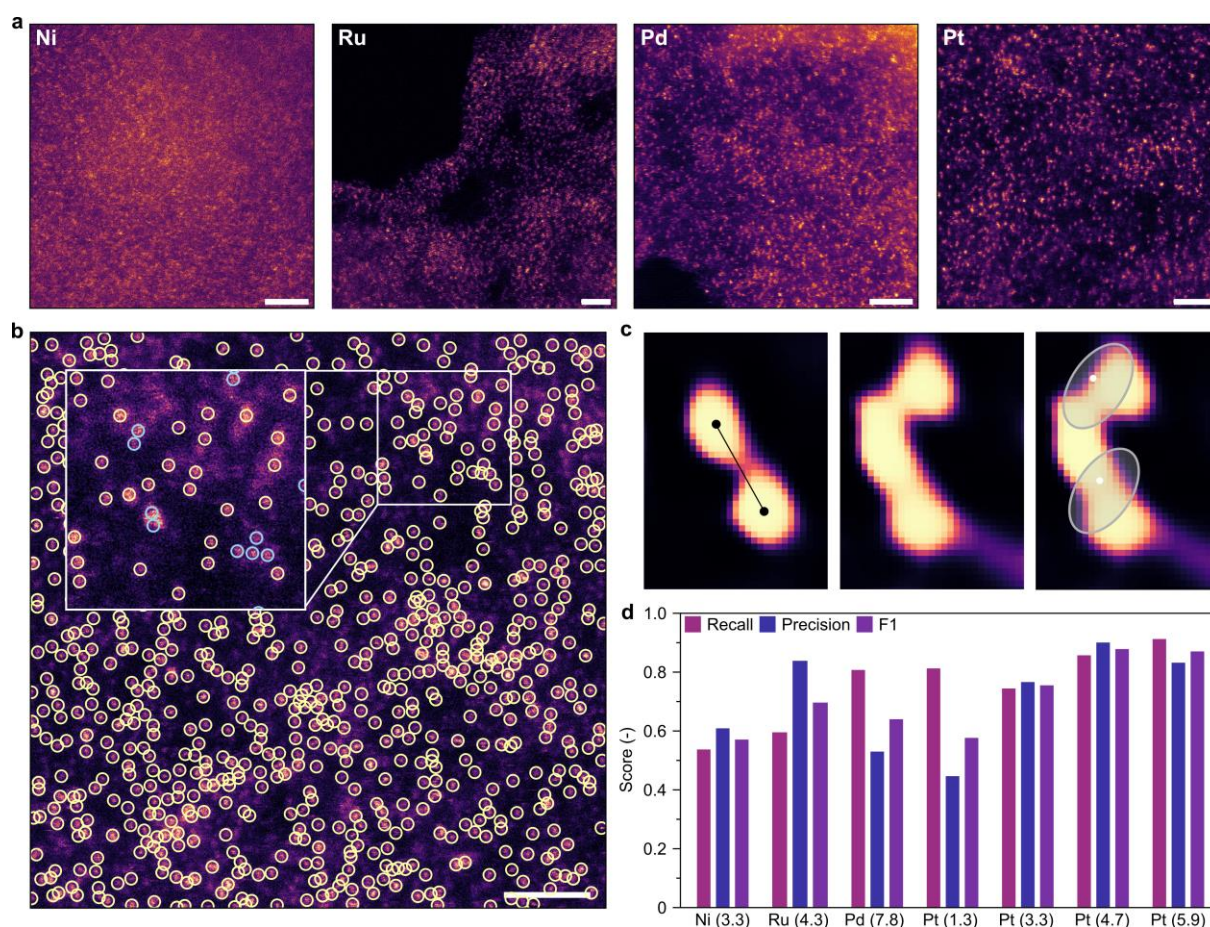
Figure 2. a, AC-STEM images of distinct UHD-SACs, illustrating the variation in contrast of the metal centers with the NC host material. All scale bars correspond to 2 nm. **b**, AC-STEM image of Pt_1/NC SAC with machine learning-detected atoms overlaid (yellow circles). The zoom inset highlights potential multimers (blue circles) that require detection and quantification. **c**, Representative prediction maps generated by the CNN for multimers assigned in **b**, exemplifying the analysis of interatomic distances (left panel) and, the use of Gaussian mixture model assignments to resolve overlapping features (central and right panels). **d**, Bar charts illustrating the performance metrics of the machine-learning model compared to manual assignments carried out by a domain expert. The comparison involved images of samples with different metal identities, density (in atoms nm^{-2}, indicated in parentheses after the metal), imaging resolutions, and measurement conditions. The (GPU accelerated) machine-learning model detections for these test images are produced in minutes, whereas the human-expert assignments took a few hours.

7

WILEY-VCH

Information) and is made available open-source and through a web-app (Figure S3, Supporting Information). The supervised step builds on a previously proposed protocol,[38] where we train a convolutional neural network (CNN) to assign a probability to each pixel in the image of whether it belongs to a metal center. A thresholding and bounding box approach then allows the identification of metal atom coordinates. New steps in this study include incorporating image intensity clipping to remove outliers during pre-processing (Figures S4 and S5, Supporting Information) and a hard-negative sampling strategy to improve the sharpness of model predictions (Figure S6, Supporting Information). Additionally, we adopt a Gaussian mixture model (GMM) to identify in an unsupervised fashion multiple atoms where features overlap in the generated prediction maps (Figure 2c, and Figure S7, Supporting Information). This approach is instrumental towards determining the fraction of metal centers associated with low-nuclearity clusters in the AC-STEM images and their respective geometries. Further, we leverage low-dimensional representation learning and unsupervised clustering to discriminate metal centers of different chemical identities in multimetallic samples (Figure S8, Supporting Information).

To minimize the need for extensive labeling of new images, we train the supervised component of the pipeline using an open-source dataset.[38] The latter consists of images of a low-density (~0.3 atoms nm^{-2}) Pt_1/NC SAC, acquired with carefully chosen and fixed imaging conditions, and including a comprehensive set of imperfections (high noise levels, emission current variations, defocus) commonly encountered when imaging SACs with AC-STEM.

To validate the transferability and accuracy of the model, we compare the machine-learning model assignments with human-expert "ground truth" assignments (Figure 2d and Figures S9-S22, Supporting Information). This comparison includes images with the highest metal atom density for each system (Ni_1/NC, Pd_1/NC, Rh_1/NC) and images with varying densities for Pt_1/NC. We assess the model accuracy and transferability using classical computer vision metrics, such as recall, precision, F1 scores, and receiver operating characteristic (ROC) curve. The comparison demonstrates satisfactory agreement across distinct metal types and atom densities (Figure 2d, and Figure S23, Supporting Information).

WILEY-VCH

In general, the performance increases with the atomic number of the metal centers, as expected due to the higher contrast exhibited by heavier atoms in AC-STEM imaging. While it was shown that the model rarely introduces false-positives in samples without metal centers,[38] the slightly lower performance for lighter atoms mirrors the inherent challenges in their detection (Figure S24, Supporting Information). Notably, this challenge was also evident to the domain-expert when labeling these images, underscoring the complexity in ensuring rigorous analysis. In this regard, the comparison of SAC descriptors derived from domain-expert and machine learning assignments will provide a holistic assessment of our automated detection pipeline's effectiveness. Initial explorations further confirm the model generality for the case of an alternative non-crystalline support, namely polymeric carbon nitride (Figures S25-26, Supporting Information).

2.2. Metal Center Organization

Following the successful validation of the improved atom detection pipeline, we perform a high-throughput analysis of the available AC-STEM images of UHD-SACs to gain quantitative insights into the spatial arrangement of the metal centers. As a first step, we measure the share of metal centers in multimer configurations based on analysis of the proximity of neighboring atoms. According to Density Functional Theory simulations (DFT) most metal dimers have intermetallic distances of 2.2 Å. Consequently, we consider a metal center to belong to a multimer if it finds any neighbor at equal or shorter distances (Figure S27, Supporting Information). The value obtained serves as an upper bound, since we cannot exclude small errors due the presence of overlapping atoms and the projection of the 3D sample into a 2D image (Figure S27, Supporting Information).

The results reveal a positive correlation between the extent of multimer formation and the surface atom density (**Figure 3a**, and Figures S28a and S29a, Supporting Information). When averaging results obtained from images of the same UHD-SAC sample, we find that the amount of non-isolated atoms is sometimes non-negligible, ranging from 0% up to 50% of the total number of detections. Since trends appear general across different metal species, we conclude that the threshold for accommodating metal centers comprising exclusively or predominantly single atoms (fewer than 5% of atoms in multimers) on the NC host studied is 1 atom nm^{-2}.

Measuring the number of atoms in each multimer reveals that dimers are the most frequent nuclearity, followed by trimers and tetramers (Figure 3c). The relative amount of atoms in multimers with nuclearity larger than 2 is typically small, in the range of 0-10%. The analysis of the number of metal-metal bonds per atom indicates that although both structures may form, clusters with a more isotropic structure are less common than chain-like geometries (Figure S30, Supporting Information). While XAS characterization is the standard technique to exclude large metal aggregates, the average nature of XAS data coupled to the detection limits make the identification of low-nuclearity metal species challenging. Our real-space analysis offers a platform for analyzing metal cluster sizes and geometrical features and confirms the absence of larger aggregates in the samples under scrutiny. By the same token, the automated detection and characterization of low-nuclearity catalysts geometrical arrangements may be instrumental to shed light on the materials chemistry and structure-property relationships beyond the single-atom regime.
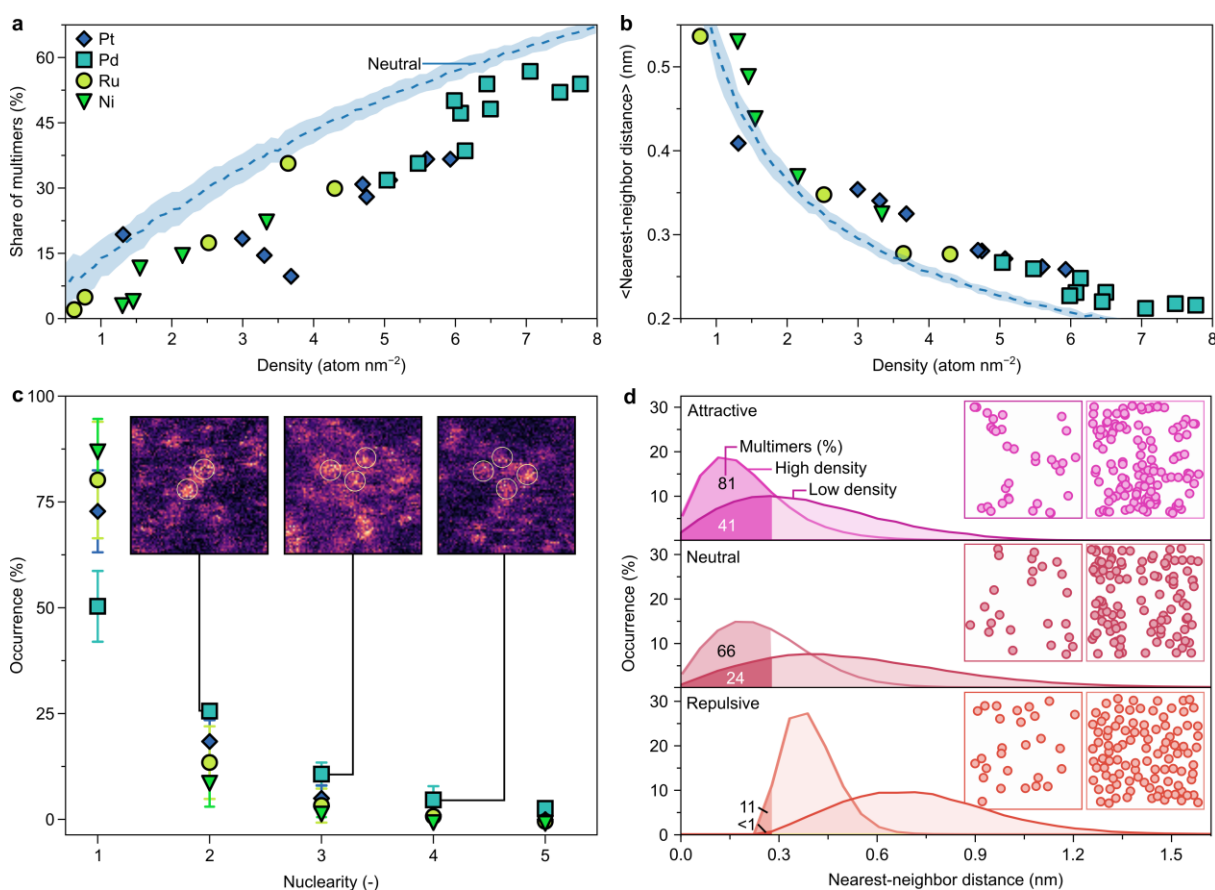
Figure 3. a, Percentage of atoms present in multimers and **b**, mean nearest-neighbor distance between metal centers detected in the automated analysis of AC-STEM images of various UHD-SACs versus atom density. We verify that similar trends also appear when considering structural descriptors derived from human-expert assignments (Figures S18 and S19, Supporting Information). The dashed lines show the expected trends from numerical models assuming a random distribution of points mediated by a neutral (null) interaction. **c**, Average distribution of multimers of a given nuclearity derived from the analysis of each UHD-SAC image available, representative examples of multimers are shown inset. **d**, Distribution of nearest-neighbor distances and share of atoms in multimers averaged over 100 independent runs for the low- and high-density cases illustrated under the assumption of attractive, neutral, or repulsive interactions. Inset display example regions of the numerical sampling accounting for attractive, neutral, or repulsive interactions on the spatial organization of randomly arranged metal centers.

Following the characterization of metal center dispersion, metal atom organization can be further analyzed in terms of the nearest-neighbor distance distributions between metal centers (NND) and their mean value (<NND>). Indeed, the latter has been proposed as a descriptor to rationalize UHD-SACs reactivity.[10,18] We report this observable for each of the analyzed AC-STEM images as a function of the atom surface density (Figure 3c, and Figures S28b and S29i, Supporting Information), evidencing an inverse correlation between the mean nearest-neighbor distances and densities. At a surface density of 1 atom nm^{-1} the <NND> is 0.50 ± 0.05 nm. This quantity sharply decreases to 0.25 ± 0.02 nm at a surface density equal to or larger than 6 atoms nm^{-1}. By examining the pair distance distribution functions among all the metal centers, we establish the absence of short- or long-range ordering in the metal center spatial organization (Figure S31, Supporting Information). When contrasting trends for systems of different composition, no significant discrepancies appear. This result suggests that, at least for the set of metal atoms considered, the spatial arrangement of metal centers on a nitrogen-doped carbon support does not depend strongly on the metal identity.

2.3. Interactions Governing Metal Center Organization

The quantitative characterization of a statistically relevant number of images and metal centers provides a platform to interrogate the material chemistry of SACs with unprecedented detail. As a paradigmatic case study, we test the theory that the metal centers' spatial arrangements in UHD-SACs are random, a hypothesis occasionally used to model the spatial organization of metal centers.[38-40] Indeed, when the number of metal atoms is much lower than the number of coordination sites, random spatial arrangements are likely to be observed if there is no preferential ordering of the coordination sites or adsorption of metal centers, which is the case for the NC host. Yet, the validity of this assumption in samples with high metal content, where metal atoms occupy almost if not all the coordination sites present and repulsive or attractive interactions may occur, has remained unproven so far.

To this end, we conduct a preliminary numerical analysis (see Methods) and sample random distributions of points (representing metal centers) on a 2D grid (representing the support). Estimation of the share of non-isolated atoms (**Figure 3a**) in the 1-8 atom nm^{-2} surface atom density range, reveals that the proportion of atoms in low-nuclearity clusters determined from analysis of the UHD-SACs is consistently lower than that anticipated by numerical models. Comparative analysis of the mean nearest-neighbor distance (Figure 3b) shows that the experimentally observed <NND> is larger than the one corresponding to a purely random model distribution, indicating that additional factors likely influence the organization. Consideration of two additional scenarios introducing an attractive or a repulsive term, reveals that such interactions can significantly affect the atom arrangement (Figure 3d). The nearest-neighbor distance distributions are centered at and spread over shorter (attractive interaction) or longer (repulsive interaction) distances with respect to the neutral case. We conclude that an apparent repulsive interaction mediates the disordered spatial arrangements of metal centers in UHD-SACs. The relationships that link surface atom density, <NND>, and the proportion of atoms in multimers, hold regardless of the metal type. For this reason, we hypothesize that the interatomic interactions governing the spatial arrangement of the host coordination sites are key to rationalize the apparent repulsion between metal centers. We then resort to DFT simulations to screen energetic trends, geometric and electronic structure effects, and to assess their role in determining the apparent repulsion between SACs metal centers.

For a comprehensive analysis, we consider diverse host coordination site geometries and perform DFT minimization of more than 800 different configurations, describing the bare NC carrier with one or multiple coordination sites and one or more metal atoms adsorbed. To assess the likelihood of observing dimers experimentally, we probe the formation energy of dimers from the gas phase (simulating the adsorption process) or from isolated metal centers adsorbed in a coordination site (simulating formation due to metal centers mobility). We find that dimerization is generally less favorable than the formation of isolated metal centers. Nevertheless, alternative synthetic pathways might lead to dimer formation (**Figure 4a** and Figure S32, Supporting Information). These configurations would likely form, after all the host coordination sites coordinate a single metal atom, if a surplus of metal precursor is available.

For additional insight into the driving forces determining metal center organization, we probe the energetic landscape of a nitrogen-doped carbon sheet containing two separate coordination sites as a function of their distance (Figure 4b and Figures S33 and S34, Supporting Information). We observe that coordination sites which share a N-N bond are highly unfavorable, while an inter-coordination site separation of around 5 Å corresponds to the minimum energy configuration. We rationalize energetic trends in terms of geometric and electronic effects (Figure 4c and Figure S33, Supporting Information), which are consistent in all the coordination site geometries considered. Also, we verify that trends hold when metal centers (Figure S35, Supporting Information) or precursors in the form of metal-ligand complexes are adsorbed (Figure S36, Supporting Information).

From the DFT simulations, we determine that the apparent repulsion in the spatial organization of metal centers in UHD-SACs stems from i) the unfavorable formation of multimers compared to isolated metal centers and ii) the energetic preference for coordination sites in a nitrogen-doped carbon carrier to lie at a distance of ~5 Å. These driving forces are sizable when the support possesses abundant coordination sites, and almost all adsorb isolated metal atoms. Vice versa, they will be vanishingly small when the synthetic route results in lower surface atom densities. Numerical models accounting for driving forces biasing the metal center organization
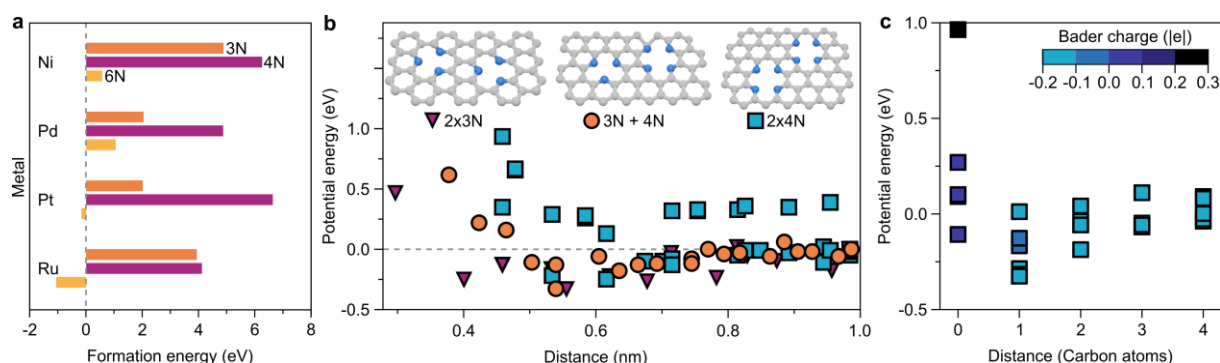
Figure 4. a. Dimer formation energy from two adsorbed isolated metal centers in M_1/NC (M = Pt, Pd, Ru, Ni) SACs as a function of the coordination site geometry and metal center species. 3N, 4N, and 6N label square-planar, trigonal, and hexagonal coordination site geometries, respectively. **b**, Dependence of the potential energy of neighboring coordination sites in an NC carrier on their separation. Energies are renormalized with respect to the one of the system with the furthest arrangement of the two coordination sites. **c**, Dependence of the potential energy of neighboring square-planar coordination sites (2×4N) in an NC carrier on the number of C atoms separating the nitrogen coordination sites and on the comparative electron charge density redistribution to the N atoms.

towards disorder arrangements and for the energetic trends inferred from DFT calculations (see Methods) support this conclusion (Figure S37, Supporting Information).

2.4. Chemically-Specific Spatial Arrangements

Allowing for the presence of metal centers of multiple chemical species in SACs gives rise to opportunities for tuning their properties, but also increases the challenges in their structural characterization. Here we show how the synergy between supervised and unsupervised methods allows to capture the additional complexity in the description of multimetallic SACs structure, enabling chemically-specific assignments of elemental labels to each metal center, provided they display differences in contrast.

As a demonstrative case, we focus on bimetallic Ni_1Pd_1/NC samples. A coarse characterization of these sample by means of energy-dispersive X-ray spectroscopy (EDX) suggested intermixing of the two chemical species, yet an atomic and chemically-specific resolution of the metal centers spatial organization was not accessible through EDX or electron energy loss spectroscopy (EELS).[12]

For this system, we validate our approach by observing the good consistency between the atom detection, element labels, and signal intensity, for assignments made by the machine learning
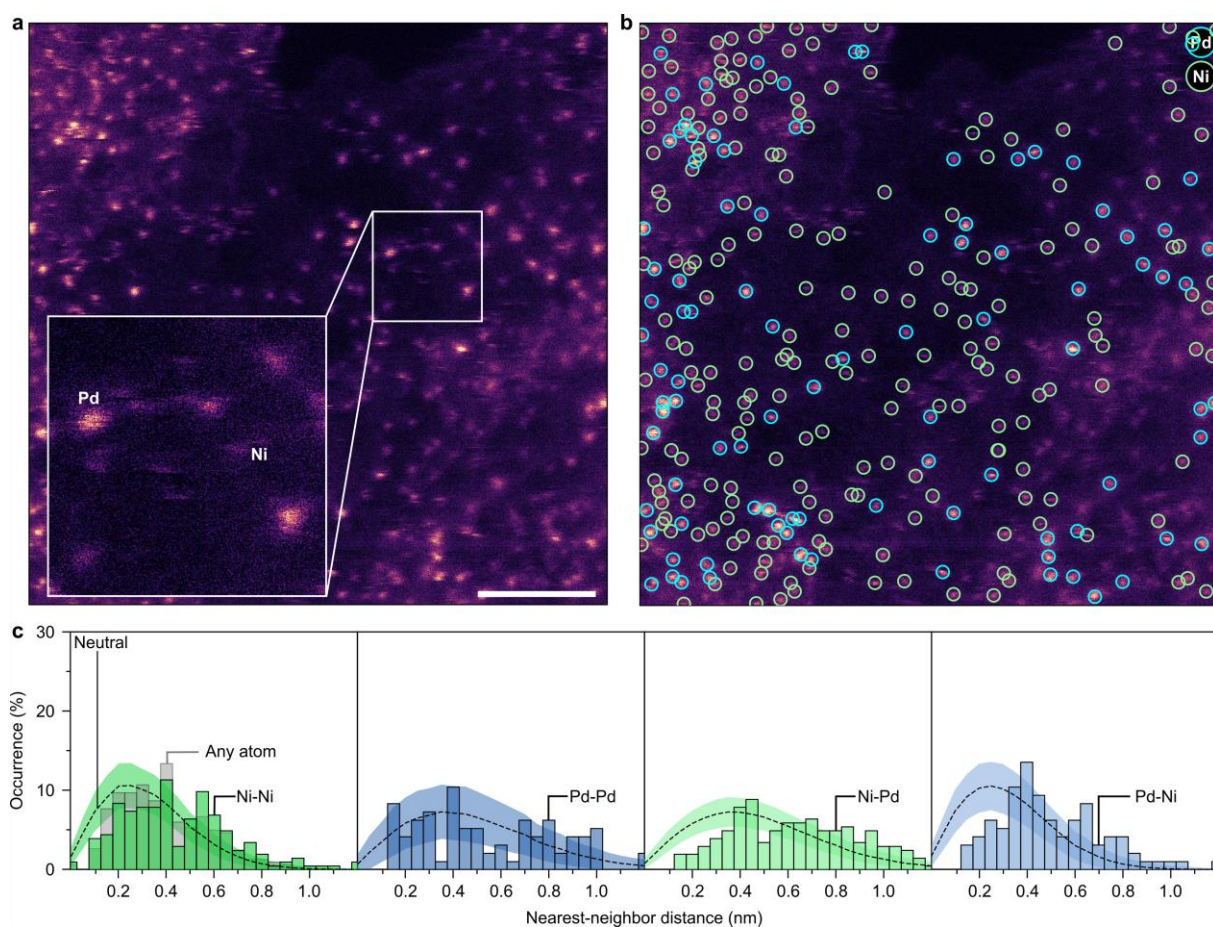

Figure 5. a, AC-STEM image of a bimetallic Ni_1Pd_1/NC. The inset illustrates the difference in contrast between Ni and Pd atoms **b**, corresponding atomic position assignments inferred by the CNN model, where atom chemical identity is predicted by the variational autoencoder latent space clustering approach. **c**, Breakdown of nearest-neighbor distance distributions when accounting for any possible neighbors (gray) or when considering element-specific pairs in a multimetallic Ni_1Pd_1/NC SAC. The

dashed line shows statistics for two non-interacting species A and B on a finite-size grid, where A and B have the same atom density of Ni and Pd, respectively.

pipeline and by a human expert (**Figure 5a-b**, and Figures S8 and S38, Supporting Information). Following the atom detection and labeling, we compare the nearest-neighbor distributions for Ni-Ni, Ni-Pd, Pd-Ni, and Pd-Pd metal center pairs with the ones found for a corresponding random distribution of two species A and B on a 2D grid (see Methods). As for the monometallic UHD-SACs, the experimental nearest-neighbor distance distributions find a peak of similar magnitude to the one predicted for a random spatial arrangement with the same total atom density, but slightly off-shifted to larger distances (Figure 5c, and Figure S39, Supporting Information). The latter observation represents an additional manifestation of the repulsive character mediating the organization of metal centers. The former result indicates the absence of preferential arrangement of Pd and Ni atoms. This outcome parallels that of the DFT simulations, where we observe similar energy trends in the adsorption of Pd or Ni atoms in the neighborhood of one another (Figure S40, Supporting Information). Extending the analysis to a trimetallic $Ni_1Pd_1Pt_1/NC$ sample, we also verify the absence of chemical ordering in this system (Figure S41, Supporting Information).

These key studies illustrate how automated metal center detection, endowed with a chemical accuracy, paves the way to the rigorous determination of potential chemical ordering in the arrangement of metal centers, beyond circumstantial or qualitative evidence. Furthermore, these characterizations highlight the heterogeneity in the adsorption site local environments present in bi- and multi-metallic SACs. Different numbers of neighbors, of the same or different chemical species, distributed over a variety of distances, are consistently observed. This knowledge, in turn, will play a key role for more precisely rationalizing, modelling, and predicting SACs catalytic properties.

3. Conclusions and Outlook

This work establishes a new paradigm in characterizing the structure of single-atom catalysts, moving away from a qualitative analysis to a systematic and quantitative description using microscopy,

WILEY-VCH

machine-learning, and numerical methods. We introduced methods for the automated detection of metal centers in AC-STEM images, enabling accurate quantification of advanced structural descriptors, such as the fraction of low-nuclearity metal clusters present, their size and geometries, the proximity and pair-distance distributions of isolated metal centers, with chemical specificity. Additionally, systematic density functional theory screening provided insights into the geometric and electronic structure contributions governing coordination sites and metal center spatial organization.

By analyzing geometric and electronic structure descriptors, we establish criteria for achieving surface isolation, and elucidate the repulsive interaction that mediates the spatial arrangement of metal centers in UHD-SACs supported on a N-doped carbon host. Extending our analysis to bi- (Ni_1Pd_1/NC) and multi- ($Ni_1Pd_1Pt_1$/NC) metallic systems offering quantitative evidence for the absence of preferential ordering in these systems.

We foresee that the ability to efficiently access an array of descriptors of SAC structures will play a pivotal role in advancing not only our fundamental understanding of the materials chemistry of SACs but also in facilitating the inference and engineering structure-property relationships. Our characterization highlights the heterogeneity in the UHD-SACs metal centers local environments, a crucial consideration when rationalizing or predicting their catalytic properties.

While challenges persist in systematic high-quality imaging of SACs, we anticipate that ongoing developments and the synergy between automated calibration, image acquisition, and atom detection will pave the way for advances. Furthermore, unbiased and automated methods, combined with collaborative community efforts and benchmarks, will improve characterization standards and enable the analysis of complex scenarios. These include tridimensional detection of metal centers distributed over three-dimensional host materials. Finally, as this work provides insights into the spatial arrangement of metal centers, we foresee the development of tailored machine learning algorithms to extract atomistic details of metal-coordination site motifs from microscopy or spectroscopy.

4. Methods

WILEY-VCH

Catalyst Synthesis: M_1/NC UHD-SACs (M_1 = Ni, Ru, Pd, Pt or combinations thereof) presented in this study were prepared following a two-step annealing method previously described,[12] using a nitrogen-doped carbon (NC) carrier derived from carbonized ZIF-8. The ZIF-8 initial template ensures high N-content and surface area, which in turn lead to the formation many coordination sites, that could host a large amount of isolated metal atoms. The two-step annealing protocol further provides a robust route towards metal center isolation also at high metal loadings. For the multimetallic systems, the metal precursors were deposited on the carrier simultaneously. The corresponding metal contents are indicated in Table S2, Supporting Information.

Scanning Transmission Electron Microscopy: An aberration-corrected JEOL ARM-200F system equipped with a cold field emission gun was exploited to perform the SAC imaging. All images were collected with a half-angle range between 80 to 280 mrad, while the convergence semi-angle was fixed at circa 30 mrad. The microscope acceleration voltages were adjusted between 80 and 200 kV for optimal contrast (see Figure S2b, Supporting Information, for parameter summary). For reference, we recall that the intensity of the signal in AC-STEM measurement is approximately correlated with the square of the atomic number Z of the probed atoms. Depending on the specific sample type and damage mechanisms, prolonged acquisition times may induce structural alterations and charging effects, which can lead to image artifacts and unrepresentative observations.

Atomic positions in all images were assigned manually and revised three times, by considering independent visualizations and zoom-ins; these positions served as "ground truths" for the machine learning model benchmarking. More than 8000 metal centers and corresponding coordinates have been identified by the human-expert during this process. We recall here that visual perception of the human is affected by numerous factors and detection criteria may be non-trivially expressed in mathematical expressions. Partial disagreement between the automated atom detection and the labels proposed by a human-expert is then tolerated, since inconsistent assignments might occur also among domain experts. The segmentation of the sample area from the background was performed by thresholding, where the value was optimized for each image.

Automated Atom Detection: As the cornerstone in the detection of metal centers we build a supervised machine learning model to classify whether crops of a determined size contain a metal

WILEY-VCH

atom or not. This design choice is motivated by the need of i) avoiding overfitting to training images, since a model might memorize the locations of the atoms in each image, rather than learning how to detect each distinct atom therein, ii) ensuring transferability of the process to new data of different sizes and resolutions, iii) requiring only visual patterns of its neighborhood to detect metal centers, and iv) simplifying the optimization criteria of the task to those of traditional classification, which is well studied. The training workflow consists of 5 steps (Figure S2a, Supporting Information). First, a set of training images was acquired and considered. Second, these images are analyzed by a human-expert, whose task is to annotate all metal center positions, which we consider as ground truths. Third, an image preprocessing is applied to standardize image intensities. This consists of an intensity clipping at the 99.9 percentile, followed by background subtraction and intensity normalization in the 0 to 1 range.

The final preliminary step before training the model consists in selecting the training points. Positive training crops are taken by randomly selecting 90% of the ground truth positions previously annotated by the human-expert. An equal amount of negative examples is also considered. These comprise either crops uniformly sampled in any region of the AC-STEM image 10 px away from any metal atom (75% of the total number of negative crops), or negative examples sampled from the neighborhood (exactly 18 px away in a random direction) of a metal atom (25% of the total number of negative crops). These last crops are added to the training data to increase the difficulty of the task, as classifying atoms against random parts of the image presents a less challenging case. Implementing a contrastive-like sampling of the negative crops improves the sharpness of areas around the predicted atoms and decreases unwanted blurriness in the prediction maps (Figure S6, Supporting Information).

Following these preliminary steps, a supervised model is trained on the task of classifying whether 21×21 px^2 crops find a metal atom at their center. Building on previous reports, the supervised model leverages a convolutional neural network (CNN) architecture[41] comprising three convolutional layers, followed by three fully connected layers (Table S3, Supporting Information).

During inference, the CNN model is exploited on newly acquired images, which have been appropriately pre-processed, to output for each pixel in the image the probability that a metal center is located at that particular position. To transform this map into a set of coordinates, a discretization

WILEY-VCH

step is required. For most cases, it is enough to discretize the probabilities with a threshold (0.8), and for each of the connected components, associate the bounding box center to the location coordinate of a single atom. However, in the case of multimer structures, the model may merge together in a single large area detections associated with multiple atoms. To better identify these instances, we employ a Gaussian mixture model (GMM) when a region exceeds a size of 200 px^2. The CNN output probability distributions are sampled numerically, and a GMM is used to determine the number and position of 2D Gaussians, which best fit the distribution (Figure S7, Supporting Information). The GMM centroids locations are then used as the atom coordinates. A modified Bayesian Information Criterion score is adopted, to accurately tag metal centers positions by disfavoring i) the fit of an unphysically large number of too close metal centers, ii) the fit of metal centers with unphysically large extensions.

If the sample under scrutiny is known to contain two or multiple chemical species, we adopt clustering and representation learning methods to automatically assign the elemental label to each metal center in an unsupervised fashion (Figure S8, Supporting Information). After each metal center has been identified through the CNN + GMM approach, 21×21 px^2 crops centered at each metal center coordinate are considered. Next, the crops are fed to a variational autoencoder (VAE),[42] which features rotational equivariance[43] and is tasked to re-generate these images (Table S4, Supporting Information). As a by-product of this learning exercise, the VAE evolves its latent space to encode a sensible and reduced dimensionality representation of each crop.

A Gaussian mixture model is used to identify clusters in the VAE latent space and distinguish atoms of different chemical species. Top-5 percentile median intensity statistics over crops in each cluster, are used to rank the cluster in terms of contrast, and, in turn, assign the elemental label accordingly. Indeed, for identical measurement conditions, the signal intensity is proportional to the square root of the element atomic number. For the case of Pd and Ni, for example, Pd atoms are the one with the strongest contrast, and Ni the ones with the lesser. In the Pt-Pd-Ni case, Pt atoms are instead the ones displaying the highest contrast, Ni the ones with the weakest, and Pd atoms are assigned to the cluster with the intermediate median intensity. In the current approach, a new VAE model is trained for each image being analyzed. As a potential extension, the use of a pre-trained VAE that is fine-tuned for each image can be foreseen to accelerate the atom label assignment process.

WILEY-VCH

Numerical Models and Descriptors of Spatial Arrangement: We work under the assumption that the surfaces of the UHD-SACs are predominantly flat and estimate atom densities and metal center distances projected in two dimensions. This assumption is motivated by the geometry and chemistry of the carrier, which is not expected to display large corrugations. On one hand, the densities and distances reported represent a lower bound with respect to the three dimensional one, on the other hand we verify through DFT models (Figure S27, Supporting Information) that projection errors are low (10^{-2} Å).

From the list of metal center coordinates, nearest-neighbor distances are evaluated from the full set of all pair distances. The mean nearest-neighbor distance is, by definition, evaluated by averaging over all the nearest-neighbor distances. The number of atoms, which belong to a multimer (i.e., dimer or other low-nuclearity clusters), is estimated by enumerating the atoms that find a nearest-neighbor at a distance of 2.2 Å or less.

To analyze proximity statistics in random distributions mediated by attractive, neutral, or repulsive forces in a finite-size 2D surface, we develop in-house python scripts. Random sampling is enforced by extracting coordinates on a 10×10 grid through the random.uniform generator implemented in *SciPy*.[44] When sampling multi-species distribution, the same sampling strategy is adopted, by repeating the sampling for each species under consideration. Statistics are drawn from at least 40 independent runs.

The mediation of an attractive term, on top of the random distribution is modeled by first sampling an arbitrary number of coordinates on the 10×10 grid, and, in second instance, sampling an additional number of coordinates in a 1×1 area centered at each of the coordinates selected in the first stage. Depending on the choice of the first and second amounts of coordinates sampled the attractive term may result in proximity statistics which display an extreme or small deviation from the ones of a random case. Trivially, if no coordinates are picked up during this second sampling phase, the sampling maps back to the purely random case. The example regions in Figure 3d were extracted from sampling including respectively 100 or 400 points for the low and high density case, where an initial set of 50 points was first sampled for the high-density case.

To simulate the presence of a repulsive term affecting the random distribution, we perform an iterative sampling. First a coordinate is chosen at random. A successive coordinate is proposed at random, and is selected if $R \in \{0,1\} + C < NN(d)$, where R labels a random number between 0 and 1, $NN(d)$ is the distance which would separate the proposed point to its nearest neighbor, and C is an arbitrary value, which biases the sampling of points so that only distances above the latter are accepted. The examples in Figure 3d corresponds to statistics gathered for 100 and 400 points and $C = 0.2$.

To develop a numerical model which encodes both contribution towards disordered arrangements, as well as the energetic trends observed in the DFT simulations, we again resort to an iterative sampling scheme. After the first two coordinates are chosen at random, a probability field is evaluated by multiplying one term, which biases the nearest-neighbor distance distribution to match a Rayleigh distribution, with another one, which approximates the population distribution inferred from DFT energetics. The next points are then chosen randomly, according to the weighted probability field, the latter is then also updated to account for the presence of the newly selected point.

DFT Simulations: Density functional theory (DFT) simulations are performed via the Vienna ab initio simulation Package (VASP 5.4.4).[45] Generalized gradient approximation with the Perdew-Burke-Ernzerhof (GGA-PBE)[46] functional is used to evaluate the exchange-correlation interactions. Dispersion contributions (D3)[47] are accounted for and spin polarization is allowed for single-atom simulations. Core electrons are described by projector augmented waves,[48] while valence mono-electronic states were expanded in plane waves with cut-off energy of 450 eV. For all the investigated systems, structures are relaxed using convergence criteria of 10^{-4} eV and 10^{-5} eV for the ionic and electronic steps, respectively.

With a focus on the formation energy of dimers adsorbed on an NC support, we consider a monolayer 6×9 slab of graphitic carbon (22.14 Å×25.56 Å) with a gamma-centered grid of 2×1×2 k-point grid, and tri-pyridinic (3N, here referred to as 3×N6), tetra-pyridinic (4N, here referred to as 4×N6), and hexa-pyridinic (6N, here referred to as 6×N6) coordination sites. These motifs are chosen as they provide representative and varied examples of trigonal, square-planar, and hexagonal defects (Note S1, Supporting Information). To form coordination sites, N atoms are introduced in the carbon sheet by

WILEY-VCH

replacing C atoms and saturating the valence. Representative configurations for these models are displayed in Figure 1b and Figures S27, S33, S34, Supporting Information.

To analyze the potential energy and electronic structure of NC configurations and investigate the driving forces governing proximity effects between coordination sites, we model a monolayer 6×9 slab of graphitic carbon (22.14 Å×25.56 Å) with a gamma-centered grid of 2×1×2 k-point grid and consider tri-pyridinic (3×N6) and tetra-pyridinic (4×N6) defects, respectively acting as representatives of trigonal and square-planar geometries. Similar to the dimer case, carbon atoms are substituted with nitrogen ones and saturating the valence. We consider three sets of NC sheets, which combine 3×N6 and/or 4×N6 coordination sites, namely, i) 3×N6-3×N6, ii) 4×N6-4×N6 and iii) 3×N6-4×N6. Simulations are performed solely on symmetry-inequivalent structures. Example configurations are reported in Figure 4b for reference. To generate sets of configurations with two coordination sites, first we consider one, containing a single coordination site, which acts as the seed structure. Next, we construct a second coordination site with distances between coordination sites ranging from the minimum possible (3 Å to 4 Å depending on the coordination site geometry) to 9 Å.

We perform Bader charge analysis on the electronic charge density distributions of all the bare NC structures.[49] To assess in a quantitative and interpretable fashion the changes in the electronic charge density as a function of the distance between the two coordination sites, we consider the descriptor <*B*>, which was evaluated by averaging the Bader charge of the nitrogen atoms in the seed coordination site. We then report on the difference in charge density between <*B*> and the charge density of nitrogen atoms in the minimum energy crystalline phase.

While GGA PBE functional is a well-established and informative modeling choice, we acknowledge that the electron density distribution may exhibit over delocalization in these simulations. To address this, we performed an analysis on a select but representative set of structures accounting for a Hubbard U term.[50] Since selecting U values is non-trivial for N-doped carbon supports, we evaluated a range of different strengths.[51,52] Our findings (Figure S34a, Supporting Information) indicate that there is no qualitative difference between the results obtained from GGA PBE calculations and those including a U term. This reinforces the robustness of the conclusions drawn from the GGA PBE approach.

WILEY-VCH

To investigate the adsorption trends of the metals under study at different distances, Ni, Pd, Pt and Ru single atoms were placed in the center of one (M/4×N6-4×N6) or both (M/4×N6-M/4×N6) coordination sites for the 4×N6-4×N6 subset. Example configurations are reported in Figures S34, S36 and S40, Supporting Information.

To assess the adsorption energy of Ni or Pd metal atoms, as a function of the presence and distance of Ni or Pd metal atoms hosted at a neighboring coordination site, we measure the E_{int} quantity. For square-planar and trigonal coordination sites E_{int} is calculated as:

$E_{int,sq} = E(\text{M/4×N6-M/4×N6}) + E(\text{4×N6-4×N6}) - 2E(\text{M/4×N6-4×N6})$

$E_{int,tr} = E(\text{M/3×N6-M/3×N6}) + E(\text{3×N6-3×N6}) - 2E(\text{M/3×N6-3×N6})$

For the mixed coordination sites, E_{int} is equal to:

$E_{int,mix} = E(\text{M/3×N6-M/4×N6}) + E(\text{3×N6-4×N6}) - E(\text{M/3×N6-4×N6}) - E(\text{3×N6-M/4×N6})$

In the presence of two different chemical species, two possible E_{int} are distinguished:

$E_{int,mix}^{AB} = E(\text{M}^A\text{/3×N6-M}^B\text{/4×N6}) + E(\text{3×N6-4×N6}) - E(\text{M}^A\text{/3×N6-4×N6}) - E(\text{3×N6-M}^B\text{/4×N6})$

$E_{int,mix}^{BA} = E(\text{M}^B\text{/3×N6-M}^A\text{/4×N6}) + E(\text{3×N6-4×N6}) - E(\text{M}^B\text{/3×N6-4×N6}) - E(\text{3×N6-M}^A\text{/4×N6})$

Supporting Information

Supporting Information is available from the Wiley Online Library or from the author.

Data Availability

The code for automated atom detection is distributed under an MIT license and can be found at https://gitlab.hpai.bsc.es/atoms/stem_atoms. The atom-detection inference pipeline is also

WILEY-VCH

accessible through a web-app hosted at https://atom-detection.nccr-catalysis.ch/. The data that support the plots within this paper are available on Zenodo https://doi.org/10.5281/zenodo.8095964 as raw files. All inputs, and output structures related to the DFT simulations are stored and accessible in the ioChem-BD repository https://iochem-bd.iciq.es/browse/review-collection/100/60773/fbc8c21a2f6517ff18652c30.

Competing Interests

The authors declare no competing interests.

Received: ((will be filled in by the editorial staff))

Revised: ((will be filled in by the editorial staff))

Published online: ((will be filled in by the editorial staff))

WILEY-VCH

References

[1]   A. Wang, J. Li, T. Zhang, *Nat. Rev. Chem.* **2018**, *2*, 65.

[2]   S. K. Kaiser, Z. Chen, D. Faust Akl, S. Mitchell, J. Pérez-Ramírez, *Chem. Rev.* **2020**, *120*, 11703.

[3]   X. Cui, W. Li, P. Ryabchuk, K. Junge, M. Beller, *Nat. Catal.* **2018**, *1*, 385.

[4]   H.-Y. Zhuo, X. Zhang, J.-X. Liang, Q. Yu, H. Xiao, J. Li, *Chem. Rev.* **2020**, *120*, 12315.

[5]   D. Faust Akl, D. Poier, S.C. D'Angelo, T.P. Araújo, V. Tulus, O.V. Safonova, S. Mitchell, R. Marti, G. Guillén-Gosálbez, J. Pérez-Ramírez, *Green Chem.* **2022**, 24, 6879.

[6]   A. K. Datye, G. Hua, *Nat. Commun.* **2021**, *12*, 895.

[7]   Y. Wang, H. Su, Y. He, L. Li, S. Zhu, H. Shen, P. Xie, X. Fu, G. Zhou, C. Feng, D. Zhao, *Chem. Rev.* **2020**, *120*, 12217.

[8]   Q. Wang, X. Zheng, J. Wu, Y. Wang, D. Wang, Y. Li, *Small Struc.* **2022**, *3*, 2200059. [9]   V. Giulimondi, S. Mitchell, J. Pérez-Ramírez, *ACS Catal.* **2023**, *13*, 2981.

[10]   Y. Chen, J. Lin, Q. Pan, X. Liu, T. Ma, X. Wang, *Angew. Chem. Int. Ed.* **2023**, DOI: 10.1002/anie.202306469.

[11]   R. Li, D. Wang, *Adv. Energy Mater.* **2022**, *12*, 2103564.

[12]   X. Hai, S. Xi, S. Mitchell, K. Harrath, H. Xu, D. Faust Akl, D. Kong, J. Li, Z. Li, T. Sun, H. Yang, Y. Cui, C. Su, X. Zhao, J. Li, J. Pérez-Ramírez, J. Lu, *Nat. Nanotechnol.* **2022**, *17*, 174.

[13]   Z. Li, B. Li, Y. Hu, X. Liao, H. Yu, C. Yu, *Small Struc.* **2022**, *3*, 2200041.

[14]   Z. Jin, P. Li, Y. Meng, Z. Fang, D. Xiao, G. Yu, *Nat. Catal.* **2021,** *4*, 615.

[15]   H. Jin, P. Cui, C. Cao, X. Yu, R. Zhao, D. Ma, W. Song, *ACS Catal.* **2023**, *13*, 1316.

[16]   H. Wang, J. X. Liu, L. F. Allard, S. Lee, J. Liu, H. Li, J. Wang, J. Wang, S.H. Oh, W. Li, M. Flytzani-Stephanopoulos, *Nat. Commun.* **2019**, *10*, 3808.

WILEY-VCH

[17]   I. Ro, J. Qi, S. Lee, M. Xu, X. Yan, Z. Xie, G. Zakem, A. Morales, J. G. Chen, X. Pan, D. G. Vlachos, *Nature* **2022**, *609*, 287.

[18]   H. Li, L. Wang, Y. Dai, Z. Pu, Z. Lao, Y. Chen, M. Wang, X. Zheng, J. Zhu, W. Zhang, R. Si, *Nat. Nanotechnol.* **2018**, *13*, 411.

[19]   A. Guan, Z. Chen, Y. Quan, C. Peng, Z. Wang, T. K. Sham, C. Yang, Y. Ji, L. Qian, X. Xu, G. Zheng, *ACS Energy Lett.* **2020**, *5*, 1044.

[20]   J. Gu, M. Jian, L. Huang, Z. Sun, A. Li, Y. Pan, J. Yang, W. Wen, W. Zhou, Y. Lin, H. J. Wang, *Nat. Nanotechnol.* **2021**, *16*, 1141.

[21]   H. Jin, R. Zhao, P. Cui, X. Liu, J. Yan, X. Yu, D. Ma, W. Song, C. Cao, *J. Am. Chem. Soc.* **2023**, *145,* 12023.

[22]   L. Han, H. Cheng, W. Liu, H. Li, P. Ou, R. Lin, H. T. Wang, C. W. Pao, A. R. Head, C. H. Wang, X. Tong, *Nat. Mater.* **2022**, *21*, 681.

[23]   V. Giulimondi, A. Ruiz-Ferrando, A. H. Clark, S. K. Kaiser, F. Krumeich, A. J. Martín, N. López, J. Pérez-Ramírez, *Adv. Funct. Mater.* **2022**, *32*, 2206513.

[24]   Y. Deng, Y. Guo, Z. Jia, J. C. Liu, J. Guo, X. Cai, C. Dong, M. Wang, C. Li, J. Diao, Z. Jiang, *J. Am. Chem. Soc.* **2022**, *144*, 3535.

[25]   M. Ziatdinov, O. Dyck, A. Maksov, X. Li, X. Sang, K. Xiao, R.R. Unocic, R. Vasudevan, S. Jesse, S. V. Kalinin, *ACS Nano* **2017**, *11*, 12742.

[26]   S. V. Kalinin, O. Dyck, S. Jesse, M. Ziatdinov, *Sci. Adv.* **2021**, *7*, eabd5084.

[27]   M. Ziatdinov, Y. Liu, A. N. Morozovska, E. A. Eliseev, X. Zhang, I. Takeuchi, S. V. Kalinin, *Adv. Mater.* **2022**, *34*, 2201345.

[28]   S. V. Kalinin, C. Ophus, P. M. Voyles, R. Erni, D. Kepaptsoglou, V. Grillo, A. R. Lupini, M. P Oxley, E. Schwenker, M. K. Chan, J. Etheridge, *Nat. Rev. Methods Primers* **2022**, *2*, 11.

WILEY-VCH

[29] Y. Liu, R. K. Vasudevan, K. P. Kelley, H. Funakubo, M. Ziatdinov, S. V. Kalinin, *Nat. Mach. Intell.* **2022**, *4*, 341.

[30] R. Lin, R. Zhang, C. Wang, X.Q. Yang, H. L. Xin, *Sci. Rep.* **2021**, *11*, 5386.

[31] J. Dan, X. Zhao, Q. He, N. D. Loh, S.J. Pennycook, *Microsc. Microanal.* **2022**, *28*, 3002.

[32] S. R. Spurgeon, C. Ophus, L. Jones, A. Petford-Long, S. V Kalinin, M. J. Olszta, R. E. Dunin-Borkowski, N. Salmon, K. Hattar, W.-C. D. Yang, R. Sharma, Y. Du, A. Chiaramonti, H. Zheng, E. C. Buck, L. Kovarik, R. L. Penn, D. Li, X. Zhang, M. Murayama, M. L. Taheri, *Nat. Mater.* **2021**, *20*, 274.

[33] F. Wang, T. R. Henninen, D. Keller, R. Erni, *Appl. Microsc.* **2020**, 50, 23.

[34] E. Schwenker, F. Sen, C. Ophus, T. Paulauskas, J. Guo, S. Hills, R. Klie, M. K. Chan, *Microsc. Microanal.* **2018**, *24*, 510.

[35] R. Girod, T. Lazaridis, H. A. Gasteiger, V. T. Tileli, *Nat. Cat.* **2023**, *6*, 383.

[36] S. Liu, H. Xu, D. Liu, H. Yu, F. Zhang, P. Zhang, R. Zhang, W. Liu, *J. Am. Chem. Soc.* **2021**, *143*, 15243.

[37] H. Ni, Z. Wu, X. Wu, J. G. Smith, M. J. Zachman, J.-M. Zuo, L. Ju, G. Zhang, M. Chi, *Nano Lett.,* **2023**, *23*, 7442.

[38] S. Mitchell, F. Parés, D. Faust Akl, S. M. Collins, D. M. Kepaptsoglou, Q. M. Ramasse, D. Garcia-Gasulla, J. Pérez-Ramírez, N. López, *J. Am. Chem. Soc.* **2022**, *144*, 8018.

[39] M. Utlaut, *Phys. Rev. B* **1980**, *22*, 4650.

[40] E. Vorobyeva, E. Fako, Z. Chen, S.M. Collins, D. Johnstone, P. A. Midgley, R. Hauert, O. V. Safonova, G. Vilé, N. López, S. Mitchell, J. Pérez-Ramírez, *Angew. Chem. Int. Ed.* **2019**, *131*, 8816.

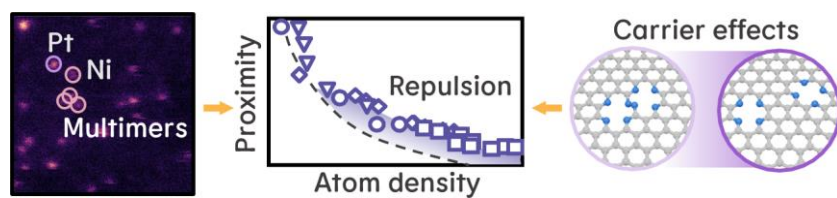[41] Y. LeCun, L. Bottou, Y. Bengio, P. Haffner, *Proc. IEEE* **1998**, *86*, 2278.

WILEY-VCH

[42]   D. P. Kingma, M. Welling, *Found. Trends Mach. Learn.* **2019**, *12*, 307.

[43]   M. Ziatdinov, C. Y. Wong, S. V. Kalinin, *arXiv preprint, arXiv:2106.12472*, submitted: May, **2021**.

[44]   P. Virtanen, R. Gommers, T. E. Oliphant, M. Haberland, T. Reddy, D. Cournapeau, E. Burovski, P. Peterson, W. Weckesser, J. Bright, S. J. Van Der Walt, *Nat. Methods* **2020**, *17*, 261.

[45]   G. Kresse, J. Furthmüller, *Comput. Mater. Sci.* **1996**, *6*, 15.

[46]   J. P. Perdew, K. Burke, M. Ernzerhof, *Phys. Rev. Lett.* **1996**, *77*, 3865.

[47]   S. Grimme, S. Ehrlich, L. Goerigk, *J. Comput. Chem.* **2011**, *32*, 1456.

[48]   G. Kresse, D. Joubert, *Phys. Rev. B* **1999**, *59*, 1758.

[49]   W. Tang, E. Sanville, G. Henkelman, *J. Phys.: Cond. Mat.* **2009**, *21*, 084204.

[50]   S. L. Dudarev, G. A. Botton, S. Y. Savrasov, C. J. Humphreys, A. P. Sutton, *Phys. Rev. B*, **1998**, *57*, 1505.

[51]   M. Cococcioni, S. De Gironcoli, *Phys. Rev. B* **2005**, *71*, 035105.

[52]   M. Capdevila-Cortada, Z. Łodziana, N. López, *ACS Catal.* **2016**, *6*, 8370.

Advancing the design of single-atom catalysts requires reliable tools for discerning distinct metal center arrangements. This study leverages state-of-the-art microscopy, machine learning, and simulations to gain insights into the organization and interactions of metal centers and coordination sites in nitrogen-doped carbons. The findings highlight the impact of density- and support-mediated repulsive interactions in shaping spatial configurations and forming low-nuclearity species.

K. Rossi, A. Ruiz-Ferrando, D. Faust Akl, V. Gimenez Abalos, J. Heras-Domingo, R. Graux, X. Hai, J. Lu, D. Garcia-Gasulla, N. López*, J. Pérez-Ramírez*, S. Mitchell*

Quantitative Description of Metal Center Organization and Interactions in Single-Atom Catalysts